Monthly Notices of the ROYAL ASTRONOMICAL SOCIETY

MNRAS **488,** 5536–5550 (2019) doi:10.1093/mnras/stz2078
Advance Access publication 2019 July 30

The 2018 eruption and long-term evolution of the new high-mass Herbig Ae/Be object Gaia-18azl = VES 263

U. Munari ,[1★] V. Joshi,[2] D. P. K. Banerjee,[2] K. Čotar ,[3] S. Y. Shugarov,[4] R. Jurdana-Šepić,[5] R. Belligoli,[6] A. Bergamini,[6] M. Graziani,[6] G. L. Righetti,[6] A. Vagnozzi[6] and P. Valisa[6]

[1]*INAF Astronomical Observatory of Padova, I-36012 Asiago (VI), Italy*
[2]*Physical Research Laboratory, Navrangpura, Ahmedabad, Gujarat 380009, India*
[3]*Faculty of Mathematics and Physics, University of Ljubljana, Jadranska 19, 1000 Ljubljana, Slovenia*
[4]*Sternberg Astronomical Institute, M.V. Lomonosov Moscow State University, Moscow 119991, Russia*
[5]*Physics Department, University of Rijeka, Radmile Matejčić, 51000 Rijeka, Croatia*
[6]*ANS Collaboration, Astronomical Observatory, I-36012 Asiago (VI), Italy*

Accepted 2019 July 24. Received 2019 July 24; in original form 2019 April 13

ABSTRACT

We have been monitoring, at high cadence, the photometric and spectroscopic evolution of VES 263 following the discovery in 2018 of a brightening labelled as event Gaia-18azl. VES 263 is so far a neglected emission-line object discovered in the 1960s on objective prism plates, tentatively classified as a semiregular AGB cool giant by automated analysis of ASASSN light curves. We have discovered that VES 263 is a bona fide massive pre-main-sequence object ($\sim$12 M$_\odot$), of the Herbig AeBe type. It is located at 1.68 $\pm$ 0.07 kpc distance, within the Cyg OB2 star-forming region, and it is highly reddened [$E(B-V) = 1.80 \pm 0.05$] by interstellar extinction. In quiescence, the spectral energy distribution is dominated by the $\sim$20 000 K photospheric emission from the central B1II star, and at $\lambda \geq 6\,\mu$m by emission from circumstellar warm dust ($T \leq 400$ K). The 2018–19 eruption was caused by a marked brightening of the accretion disc around the B1II star as traced by the evolution with time of the integrated flux and the double-peaked profile of emission lines. At the peak of the eruption, the disc has a bulk temperature of $\sim$7500 K and a luminosity $L \geq 860$ L$_\odot$, corresponding to a mass accretion rate $\dot{M} \geq 1.1 \times 10^{-5}$ M$_\odot$ yr^{-1}. Spectroscopic signatures of possible bipolar jets (at -700 and $+700$ km s^{-1}) of variable intensity are found. We have reconstructed from Harvard, Moscow, and Sonneberg photographic plates the photometric history of VES 263 from 1896 to 1995.

Key words: stars: pre-main-sequence – stars: variables: T Tauri, Herbig Ae/Be – open clusters and associations: individual: Cyg OB2.

1 INTRODUCTION

On 2018 April 18, the *Gaia* team issued an alert for a 0.5 mag increase observed by *Gaia* on a field star located at (J2000) $\alpha = 20^{\rm h}31^{\rm m}48\overset{\rm s}{.}85$, $\delta = +40^\circ 38' 00\overset{''}{.}1$, rising from a previous average of $G = 12.16$ to $G = 11.66$ mag. The brightening star was logged as Gaia-18azl, and the event was also filed as AT-2018awf by the IAU Transient Name Server. On this server, a couple of days past discovery, R. Fidrich noted the presence at this position of an anonymous star recognized as a variable by the ASASSN sky patrol (and logged as ASASSN-V J203148.85+403800.1). Fidrich commented as the ASASSN automated classification of the star as a semiregular variable of $P = 197$ d seemed unlikely given the ASASSN light curve, and suggested instead it being a young stellar object in outburst.

A positional search through the literature revealed Gaia-18azl being identical with VES 263, a poorly known emission-line star catalogued by the Vatican Emission Star survey (Wisniewski & Coyne 1976), and by Stephenson & Sanduleak (1977) as SS 447. The latter noted strong Hα in emission, but said nothing about the underlying continuum. The latter was classified as that of a B star by Downes & Keyes (1988) from spectroscopic observations but with no further details or a spectrum being shown. The object was also observed as having the Hα line in emission in the course of the Hamburg Observatory objective-prism sky survey (carried

★ E-mail: ulisse.munari@oapd.inaf.it

out in 1964–70), entering the Kohoutek & Wehmeyer (1997, 1999) catalogue as HBHα 4203-31. Comerón & Pasquali (2012, hereafter CP12), in the course of a survey of the Cygnus OB2 association and its surroundings in search for previously unrecognized massive stars, obtained a low-resolution spectrum of the same object, logged as J20314885+4038001, without commenting on its positional coincidence with entries in catalogues of emission-line stars. They classified the spectrum as a highly reddened B1II star and in their plot, covering the range 3900–4900 Å (i.e. Hϵ–Hβ), no emission line is readily evident, including Hβ that looks in normal absorption without an emission core.

VES 263 lies positionally close to the centre of the massive Cygnus OB2 association, at the outskirts of the γ Cyg bright nebula and the dark cloud LDN 889 (Lynds 1962), which appears superimposed to it. Inspection of IRAS mid-IR maps shows VES 263 being at the very heart of a highly structured, knotty dust complex extending $\sim 2^{\circ}$ in radius. This is an area of intensive star formation, with the two highest mass Herbig Ae/Be stars lying close to VES 263 viz. MWC 1021 at 72 arcmin and V1478 Cyg at 14 arcmin. Herbig Ae/Be stars (HAeBes for short) are pre-main-sequence stars of intermediate mass, spanning the range between the lower mass T Tauri stars and the embedded massive young stellar objects (MYSOs). The most recent catalogue of HAeBes by Vioque et al. (2018) lists 252 entries, with only 79 of them corresponding to B- or O-spectral types and the rest being cooler/lower mass stars. The discovery of any new high-mass HAeBe object is therefore relevant given the limited number of such objects known in the whole Galaxy.

The B1II spectral type, the strong Hα feature in emission, the partnership with a site of ongoing stellar formation, and the location at the boundaries of a dark interstellar cloud perfectly match VES 263 with the classification criteria formulated by Herbig (1960) for HAeBe objects. Motivated by this, after the *Gaia* alert we initiated a high-cadence BVR_CI_C monitoring, later augmented by low- and high-resolution optical spectroscopy, near-IR observations, and a search through photographic archival repositories, the results of which are presented and discussed here. We will show how VES 263 is indeed a bona fide new HAeBe star, heavily obscured by interstellar extinction and with IR excess due to circumstellar dust, showing a complex century-long photometric history and a marked variability rapidly increasing towards the infrared, in addition to a bright circumstellar disc where double-peaked emission lines form and which is responsible for the recorded photometric variability.

2 OBSERVATIONS

2.1 Optical photometry

BVR_CI_C photometry (in the Landolt system) of VES 263 was obtained with five ANS Collaboration telescopes (with identifiers 606, 703, 1301, 1507, and 2900), all located in Italy and each working independently from all others (for simplicity, in the rest of the paper we will adopt R and I for band nomenclature instead of the more precise R_C and I_C). The operation of ANS Collaboration telescopes is described in detail by Munari et al. (2012) and Munari & Moretti (2012). The observations at each site were transformed from the instantaneous local photometric system to the standard Landolt system via a common local photometric sequence established around VES 263 and covering a wide range in colour that brackets that of the program star. An initial version of the local photometric sequence was extracted from the APASS all-sky survey

Table 1. Optical photometry of VES 263 (a small portion is shown here to provide guidance about its content: the full table is available in electronic form only). The last column lists the telescope identifier, the same as used in Fig. 1.

HJD	B	V	R	I	ID
2458488.254	14.920	13.097	12.019	11.039	606
2458489.206	14.932	13.075	12.037	11.053	1507
2458490.211	14.938	13.076	12.035	11.046	1507
2458490.253	14.927	13.088	12.041	11.054	2900

(e.g. Henden & Munari 2014) and ported to Landolt equatorial system via the transformations calibrated in Munari et al. (2014). The sequence was then continuously improved as a by-product of the accumulating observations of VES 263, and by the end of the campaign, all observations were re-reduced on the central ANS Collaboration server against this improved and final sequence. In all we collected 163 independent *BVRI* runs, on 109 different nights, from 2018 May 25 to 2019 March 30. The results are listed in Table 1 (available in full in electronic form only). The total error budget (quadratic sum of the Poissonian noise on the variable and the formal error on transformation from the local instantaneous system to the standard one via colour equations) has a median value of 0.009 mag for the data in Table 1 and it is therefore omitted. The resulting colour and light curves are plotted in Fig. 1.

2.2 Optical spectroscopy

Low-, medium-, and high-resolution spectra of VES 263 were obtained with three different telescopes located in Asiago and Varese (Italy). In all observations the spectrograph slit was aligned along the parallactic angle for optimal flux calibration, achieved by comparison against a spectrophotometric standard located close to VES 263 in the sky and observed either immediately before or after the target. Data reduction was carried out in IRAF and involved the usual steps on bias and dark removal, flat-fielding, variance-weighted spectrum tracing, sky subtraction, wavelength calibration, heliocentric correction, and flux calibration. A log of the spectroscopic observations at optical wavelengths is provided in Table 2.

The Asiago 1.22 m deployed a B&C spectrograph and ANDOR iDus DU440A camera housing a back-illuminated E2V 42-10 CCD (2048 × 512 array, 13.5 μm pixels). The low-dispersion observations of VES 263 were obtained with a 300 ln mm^{-1} grating blazed at 5000 Å, providing a dispersion of 2.31 Å/pix over the range λλ 3300–8000 Å, while medium dispersion observations used two 1200 ln mm^{-1} gratings, one blazed at 4000 Å and the other at 6500 Å both giving a dispersion of 0.60 Å/pix.

On the Asiago 1.82 m telescope, to record the high-resolution spectra of VES 263, we used the REOSC-Echelle spectrograph, which is equipped with an EEV CCD47-10 CCD (1024 × 1024 array, 13 μm pixels). It covers the interval λλ 3700–7300 Å in 30 orders without inter-order gaps. A slit width of 1.5 arcsec was used resulting in a resolving power of 20 000.

The Varese 0.84 m telescope was used in conjunction with a mk.III multimode spectrograph from Astrolight Instr., feeding light to an SBIG ST-10XME camera (2184 × 1472 array, 6.8 μm). The slit width was allowed to vary between 2 and 3 arcsec in accordance with the seeing. In the Echelle configuration, the multimode spectrograph covers the range λλ 4225–8910 Å in 27 orders, at a resolving power of 16 000 and without significant inter-

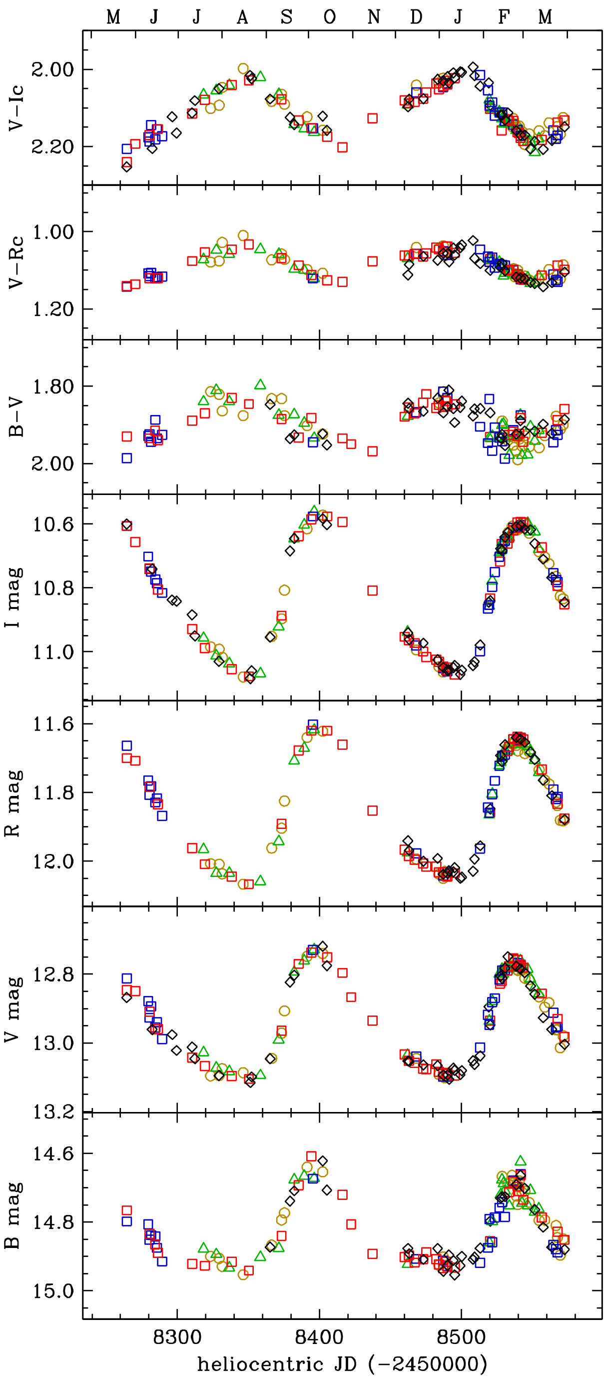

Figure 1. The BVR_CI_C light- and colour-evolution of the 2018–19 outburst of Gaia-18azl = VES 263 from our observations listed in Table 1. Data provided by different ANS Collaboration telescopes are marked with different symbols. The letters at the top mark the months from 2018 May to 2019 March.

order wavelength gaps. In the low-dispersion mode, a 600 ln mm^{-1} grating blazed at 5000 Å was adopted allowing coverage of the interval λλ 4585–9490 Å at 2.10 Å/pix.

2.3 Near-IR

NIR spectroscopy and JHK_s-band photometry of VES 263 were obtained at a few epochs with the 1.2 m telescope of the Mount Abu Infrared Observatory (Banerjee & Ashok 2012) using the Near-Infrared Camera/Spectrograph equipped with a 1024 × 1024 HgCdTe Hawaii 1 array.

In photometry, the camera provides an unvignetted 8 × 8 square arcmin field of view. Frames in each filter were obtained in five dithered positions offset typically by 30 arcsec, with five frames being obtained in each dithered position. The corrected science frames were again median combined to produce a sky frame that was subtracted from the individual science frames. Flat-field correction was applied using a sky flat derived from dark subtracted raw frames. Finally, the frames were corrected for bad pixels and cosmic ray hits. The final corrected science frames were co-added to produce an average frame on which aperture photometry was done using routines in IRAF with the 2MASS field stars J20314618+4041107, J20321252+4039474, and J20320263+4035518 used for photometric calibration. The recorded JHK_s photometry of VES 263 is given in Table 3.

A near-IR spectrum of VES 263 was obtained on 2019 December 31.603 UT at an airmass ∼2.7, covering the wavelength range 0.90–1.78 μm and at a resolution $R \sim 1000$. The star was dithered to two positions along the slit to allow for sky and dark subtraction. These sky-subtracted images were used to extract 1D spectra. Wavelength calibration, accurate to a 1σ value of 0.0002 μm, was done using a combination of OH airglow lines and telluric lines that register with the stellar spectra. To remove telluric lines and to correct for instrumental response function, the target spectra were ratioed with the spectral standard SAO 71278 (Sp. type A0V, $T_{\rm eff}$ = 9750 K), from whose spectra the hydrogen Paschen and Brackett absorption lines had been removed. The blackbody curve corresponding to the effective temperature of the spectral standard star was finally multiplied with the ratioed spectra. Data reduction and analysis were done using IRAF tasks and Python routines developed by us.

2.4 Objective prism plates

Six deep 103a-F photographic plates, exposed through a 4°5 objective prism (650 Å mm^{-1} at Hγ) on various nights of 1973 November, were found in the plate archive of the Asiago 67/92cm Schmidt telescope covering the sky around VES 263. Eye inspection through a high-quality binocular Zeiss microscope revealed Hα to be in strong emission in VES 263 at that time. The underlying continuum appears very red and the contrast of the Hα emission is compatible with a photographic rendition of the CCD spectrum shown in Fig. 4.

3 THE 2018–19 ERUPTION

3.1 Photometric behaviour

Our *BVRI* photometric monitoring of the 2018–19 eruption of VES 263, triggered by the Gaia-18azl alert, is presented in Fig. 1. The behaviour is very smooth (no noticeable short time-scale changes), with the amplitude of variation growing with increasing wavelength, from $\Delta B = 0.31$ mag to $\Delta I = 0.50$ mag.

During the current 2018–19 eruption, VES 263 is redder than in the preceding quiescence, and the variability within the eruption is characterized by redder colours when the star is brighter and bluer when fainter, in a tight correlation. This colour behaviour precludes either a variable dust obscuration or a change in photospheric temperature affecting the B1II star as the causes of the observed variability. An increase in photospheric temperature would in fact

Table 2. Log of optical spectroscopy. The last column lists the integrated absolute flux of Hα (in units of 10^{-13} erg cm^{-2} s). The symbol ‡ marks nights without observations of spectro-photometric standard stars.

Date	<UT> hh:mm	Expt sec	Disp. Å/pix	Range Å	Grating ln mm^{-1}	Tel. ID	Hα (10^{-13})
2018 Jul 29	22:10	900	ECH	3700–7300	–	1.82m	2.845
2018 Nov 18	20:17	1200	2.31	3330–8025	300	1.22m	3.625
2018 Dec 11	18:45	5400	ECH	4225–8910	–	0.84m	2.924
2018 Dec 17	16:57	900	ECH	3700–7300	–	1.82m	‡
2018 Dec 17	17:29	1800	2.31	3210–7915	300	1.22m	3.080
2018 Dec 20	18:18	5400	ECH	4225–8910	–	0.84m	2.680
2018 Dec 21	17:02	3600	0.60	7360–8585	1200R	1.22m	–
2018 Dec 22	18:00	3600	0.60	7635–8850	1200R	1.22m	–
2018 Dec 24	17:14	3600	0.60	3810–5040	1200B	1.22m	–
2018 Dec 26	17:32	3600	0.60	3810–5040	1200B	1.22m	–
2018 Dec 27	17:44	7200	0.60	3780–5017	1200B	1.22m	–
2018 Dec 27	18:09	3600	ECH	3700–7300	–	1.82m	‡
2018 Dec 29	17:55	5400	ECH	4225–8910	–	0.84m	2.618
2018 Dec 31	17:50	5400	ECH	4225–8910	–	0.84m	2.711
2019 Jan 02	18:00	5400	2.10	4585–9490	600	0.84m	2.785
2019 Jan 07	17:45	5400	2.10	4585–9490	600	0.84m	2.657
2019 Jan 25	17:27	2000	ECH	3700–7300	–	1.82m	2.502
2019 Feb 13	04:43	5400	2.10	4585–9490	600	0.84m	2.790
2019 Feb 16	03:49	3600	ECH	3700–7300	–	1.82m	3.090
2019 Feb 16	04:53	3600	2.10	4585–9490	600	0.84m	2.991
2019 Feb 17	04:05	3600	ECH	3700–7300	–	1.82m	3.021
2019 Feb 18	04:06	3600	ECH	3700–7300	–	1.82m	3.072
2019 Feb 19	04:26	3600	2.10	4585–9490	600	0.84m	3.031
2019 Feb 26	03:57	4500	2.10	4585–9490	600	0.84m	3.388
2019 Mar 06	03:48	3600	2.10	4585–9490	600	0.84m	3.860
2019 Mar 19	03:11	3600	2.10	4585–9490	600	0.84m	3.832
2019 Mar 30	03:18	3600	2.10	4585–9490	600	0.84m	3.439

Table 3. Infrared photometry of VES 263.

UT	J	H	K_s
2018 Dec 31.567	9.23 ± 0.03	8.68 ± 0.02	8.26 ± 0.03
2019 Feb 14.045	8.75 ± 0.03	8.24 ± 0.04	7.87 ± 0.04
2019 Fev 22.917	8.76 ± 0.03	8.23 ± 0.02	7.86 ± 0.03

make VES 263 brighter but also bluer over the whole λ-range. Similarly a reduction in the amount of dust extinction, if any should occur, would result in a brighter VES 263, but again in bluer colours.

To put the data for 2018–19 eruption into perspective, we have retrieved patrol data from the ASASSN archive (Shappee et al. 2014; Kochanek et al. 2017) and use them in Fig. 2 to build a longer baseline 2014–2019 V-band light curve for VES 263. The ASASSN V-filter photometry is derived differentially with respect to field stars, and no colour transformation to the standard V band is performed (M. Pawlak private communication). This may be relatively inconsequential for stars of neutral colours, but it leads to appreciable offsets for very blue or very red objects. Comparing APASS and ASASSN photometry for VES 263 in quiescence, it is obvious how the ASASSN V-filter data need the application of a −0.048 mag offset to be brought into agreement with proper V-band magnitudes. The same offset is obtained when comparing ASASSN and our data for the current outburst. Therefore a −0.048 offset is applied to the ASASSN data before plotting them in Fig. 2. The formal internal error of ASASSN data ranges from 0.011 to 0.067, with a median value of 0.015 mag.

The 2014–2017 part of the light curve in Fig. 2 shows VES 263 stable at V = 13.15, with small-amplitude and short-lived

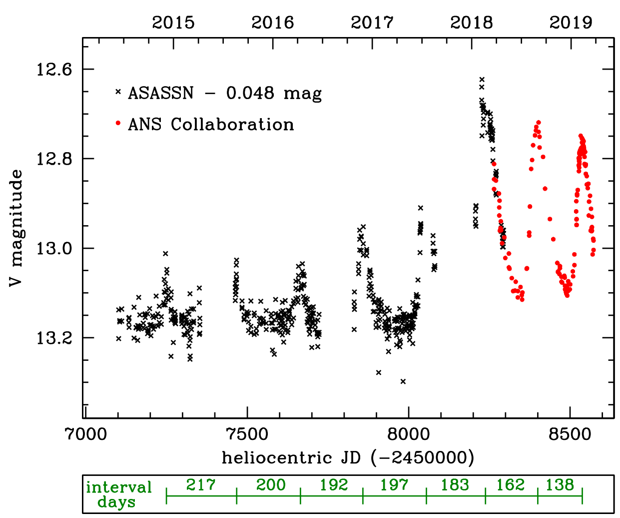

Figure 2. The recent photometric history of VES 263 constructed by combining archival V-filter photometry from the ASASSN project with current outburst V-band data from the ANS Collaboration. The latter are fully colour transformed to the Landolt system, while ASASSN are not and require the indicated −0.048 mag shift to be brought into agreement with APASS and ANS photometry.

brightenings by ΔV 0.1/0.2 mag. The following three brightenings, starting with the one noticed by *Gaia* at the beginning of 2018, are larger in amplitude and characterized by the distinctive feature that at minima the system remains brighter than in quiescence. As illustrated by the bar at the bottom of Fig. 2, the time interval between successive brightenings steeply decreases from 217 to 138 d. This precludes them being caused by changing orbital aspect in a binary system or by rotation of a heavily spotted photosphere.

The steep decrease in the time interval between successive brightenings also argues against them being caused by radial pulsations, in spite of the shape of the light curve in Fig. 1 reminiscent of Cepheid variables (and similarly for RR Lyr and Mira types). Pulsating variables are known to change in amplitude and period, but much more gradually and by smaller amounts (e.g. Sterken & Jaschek 1996). However, common to all types of radial pulsators is the fact that their colours get *bluer* on the rise in brightness, while VES 263 instead turns redder. Furthermore, VES 263 lies far away from the radial pulsation instability strip on the HR diagram (see Section 7 below), and the types of non-radial pulsating variables observed around its position on the HR diagram (i.e. 53 Per, α Cyg, β Cep) are characterized by (much) shorter periods and smaller amplitudes (as documented in the *General Catalog of Variable Stars* by Samus' et al. 2017).

In this section, we have been able to exclude various possible causes for the variability and current eruption displayed by VES 263 viz. variable dust obscuration, temperature changes, pulsations, stellar rotation, and orbital motion. The agent responsible for the observed variability seems therefore distinct from the B1II star, something appreciably cooler, and of a large size in order to match its radiation output. In the following we will argue that this is caused by a circumstellar disc.

3.2 Long-term evolution from historic photographic plates

No variability of VES 263 was noted before the recent *Gaia* trigger and the ASASSN patrol data, in spite of the convenient sky location and apparent brightness of the object. The obvious question thus concerns how unique is the present eruption in the context of the recorded history of the object. To investigate its past photometric behaviour, we turned our attention to the photographic plate stacks at Harvard, Moscow, and Sonneberg. The earliest plate imaging VES 263 that was found in them is from 1896, the latest was exposed in 1995, thus encompassing a whole century of the object's history.

With the assistance of Edward Los of the Harvard College Observatory, we accessed, prior to public release, the results of DASCH scans (Grindlay et al. 2012) of Harvard plates imaging the region containing VES 263. After culling the large number of untrustable plates, we found a total of 206 reliable DASCH measurements of VES 263 on Harvard plates, which are plotted in Fig. 3. Two of us (S.Y.S. and R.J.-S.) have directly accessed the plate archives of the Sternberg Astronomical Institute (SAI) in Moscow and of the Astronomical Observatory in Sonneberg (Germany) and looked for plates imaging VES 263. A total of 155 good blue-sensitive plates were found and measured (82 from the SAI 40 cm astrograph, and 73 from various Sonneberg astrographs). The results are given in Table 4 and included in Fig. 3. The agreement between Harvard, Moscow, and Sonneberg plates is excellent in view of the limitations inherent in photographic plates and object variability. The three sets are complementary, with the Harvard plates covering the earlier years better, while the Moscow and Sonneberg plates extend to more recent epochs, and in particular filling-in the so-called Menzel's gap (1955–1965) that affected the Harvard sky patrol. The formal error of the photographic plate measurements ranges from 0.05 to 0.2 mag (median value 0.1 mag), while the dispersion of the individual

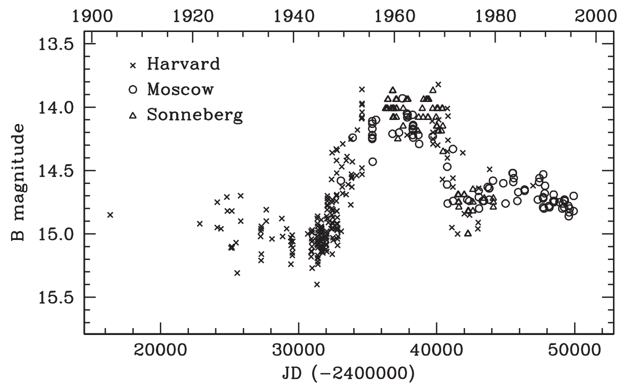

Figure 3. Historical blue-band light curve of VES 263 constructed from Harvard, Moscow, and Sonneberg photographic plates.

Table 4. *B*-band magnitude of VES 263 estimated on photographic plates taken with astrographs in Crimea (C) and Sonneberg (S). The JD column lists the geocentric JD – 240 0000 (a small portion is shown here to provide guidance about its content: the full table is available in electronic form only).

JD	*B*	Tel.
42306.437	14.82	S
42362.223	14.74	C
42630.500	14.82	S
42633.534	14.75	S
43040.477	14.66	C
43050.399	14.71	C

data points along the mean light curve in Fig. 3 is σ = 0.11 mag.

The photometric behaviour in Fig. 3 suggests VES 263 to have lingered around the quiescence *B*-band level ($B = 14.93$ according to APASS) until about 1945 when the star begun a slow rise from $B \sim 15.05$ reaching $B \sim 14.15$ by ~1953. It then remained around $B \sim 14.10$ until about 1969 when it begun a descent reaching $B \sim 14.85$ around 1972. This was followed by a resumption in brightness increase peaking at $B \sim 14.60$ by 1984 and a new descent to $B \sim 14.85$ by the time of the last photographic images exposed in 1995, with a trend suggesting a return to quiescence level by ~1998.

The average $B \sim 14.10$ level during the 1953–1969 *plateau* is far brighter than the $B \sim 14.65$ value reached at the peak of the current 2018–19 outburst. For amplitude and duration, the 1953–1969 plateau is the largest event in the recorded photometric history of VES 263. On the other hand, the rise to it has been slow and gradual, and the present 2018–19 eruption could be the start of a new activity cycle similar to that leading to the plateau of half a century ago.

For completeness, we report that in the Sternberg plate archive in Moscow we found a further 32 plates going just deep enough to have barely recorded VES 263. These blue-sensitive plates were exposed between 1896 and 1947 with two smaller astrographs located in Moscow, with lenses 10 and 16 cm in diameter. On these plates, VES 263 is seen close to the faint limit of the plates, which precludes an accurate measurement of its brightness. None the less, these plates are useful to show that VES 263 was always close to quiescence brightness during this whole period, and thus excluding any major brightening like the one recorded during the 1953–1969 plateau.

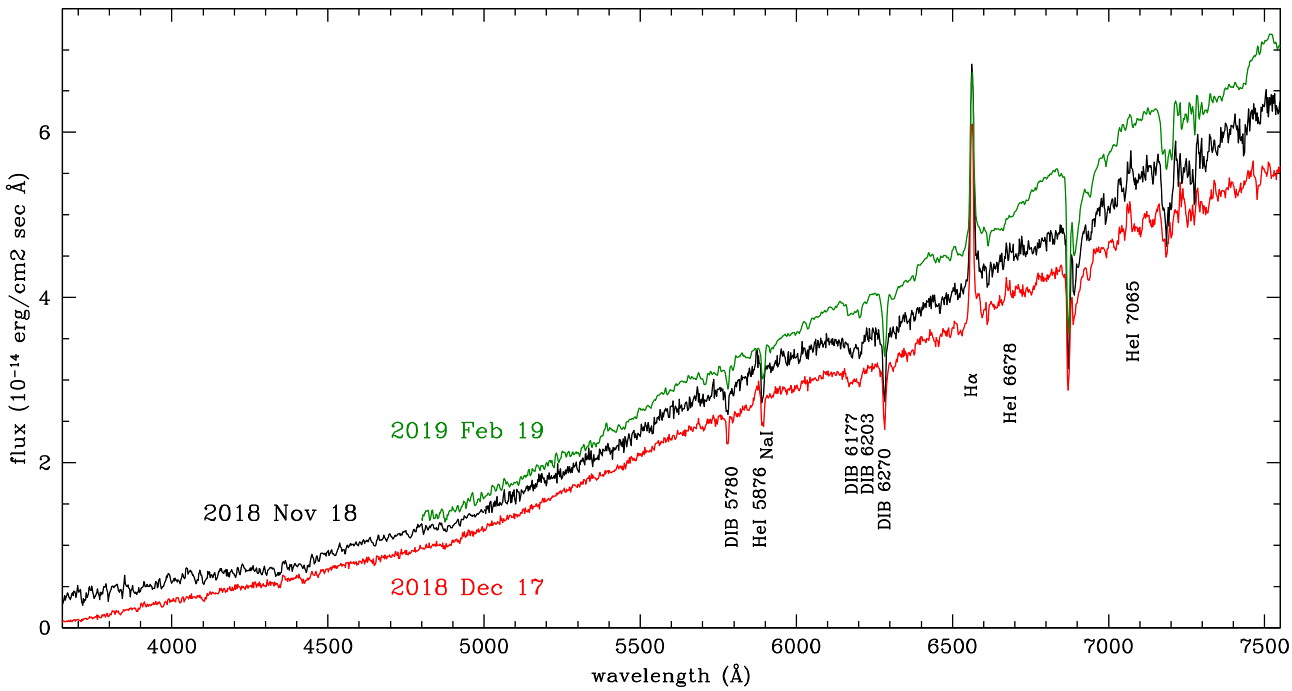

Figure 4. Sample low-resolution spectra of VES 263 for three distinct states during the 2018–19 eruption: minimum (2018 December 17), peak (2019 February 19), and intermediate brightness (2018 November 18). The strongest interstellar absorption features and stellar emission lines are identified.

3.3 Spectroscopic behaviour

A sample of the low-resolution optical spectra that were acquired for VES 263 during the 2018–19 eruption is presented in Fig. 4 corresponding to minimum, maximum, and mid-brightness. The very red slope of the continuum is obvious as is the presence of a strong Hα line in emission and also the signatures of interstellar absorption (atomic lines and DIBs). Some He I lines are seen in weak emission, 5876 and 7065 Å being the strongest.

A medium-resolution optical spectrum of VES 263 in eruption is presented in Fig. 5, focusing on the classical 3850–5000 Å interval used for spectral classification. CP12 rated their B1II classification (performed over the same 3850–5000 Å interval) as having an uncertainty negligible in the spectral type (0.5 subtypes) and larger (2 classes) in luminosity class. Consequently, in Fig. 5 we compare our spectrum of VES 263 with that of template stars for spectral types B1III, B1II, and B1I, selected from the Yamashita & Nariai (1977) list of recommended standards. They have been observed the same night with the same telescope and instrumental configuration as used for VES 263. For an easier comparison, their slopes have been forced to replicate that of the much more reddened VES 263, and have offsets added for plot clarity. The most significant interstellar atomic lines and DIBs are marked.

An immediate difference with the spectrum presented by CP12 (their fig. 2) concerns the Hβ line. The CP12 spectrum was obtained in quiescence and presents an Hβ in full absorption, while the eruption spectrum in Fig. 5 is characterized by a filled-in Hβ with a double-peaked emission profile, which is plotted on a velocity scale in the insert. In addition, the fine details of the absorption lines appear different from CP12. The redder the continuum becomes, the less pronounced are the absorption lines, as if they are veiled by continuum emission from a cooler source. This is quite obvious when comparing the intensity of He I 4026 with that of He I 4922 in VES 263 and in the template stars. The appearance of He I 4922 is significantly weakened in VES 263, while He I 4026 stands much closer to the intensity displayed in the template stars. The putative cooler source, whose emission veils weaker lines from the B1II central star, seems also to add broader wings to the Balmer lines. Such broad wings are absent in the spectra of the template stars and also in the quiescence spectrum shown by CP12 (even if the limited resolution of their plot could lead to a wrong impression here).

Just 5 d past the medium-resolution optical spectrum presented in Fig. 5, we have obtained the infrared spectrum shown in Fig. 6 and covering the *Y*, *J*, and *H* wavelength intervals. There is no trace of the B1II photospheric absorption lines, the spectrum being dominated by the continuum emission from the cooler source responsible for the photometric eruption. The Paschen and Brackett series of hydrogen appear in emission as also a fairly strong He I 1.083 µm feature. Weaker features at 1.0686 and 1.1287 µm are attributed to C I and O I. Since the O I 1.1287 µm line is significantly strengthened by Lyman continuum fluorescence (Mathew et al. 2018) and it is seen here in emission whereas the continuum fluoresced O I 1.3164 µm is not, it implies the presence of a copious source of LyC photons whose source must obviously be the hot B1II central star. Comparing the slope of the optical spectra in Fig. 4 rising towards the red with that of the infrared spectrum in Fig. 6 going the opposite way, it is evident how the peak of VES 263 observed spectral energy distribution is placed around 1.0 µm.

It is also worth noting that the Brackett lines in the *H* band are optically thick because Br10 at 1.7362 µm is weaker than the higher Brackett lines like Br11, Br12, etc., whereas it would be expected to be stronger had Case B conditions been followed for emission coming from an optically thin gas. That the H I lines are optically thick is not a surprise, since as shown in coming sections, the object is identified as an HAeBe star with a disc, and the disc in such stars, from which the H I lines originate, is expected to have high densities of 10^{11}–10^{13} cm^{-3} (Mathew et al. 2018, and references within). At

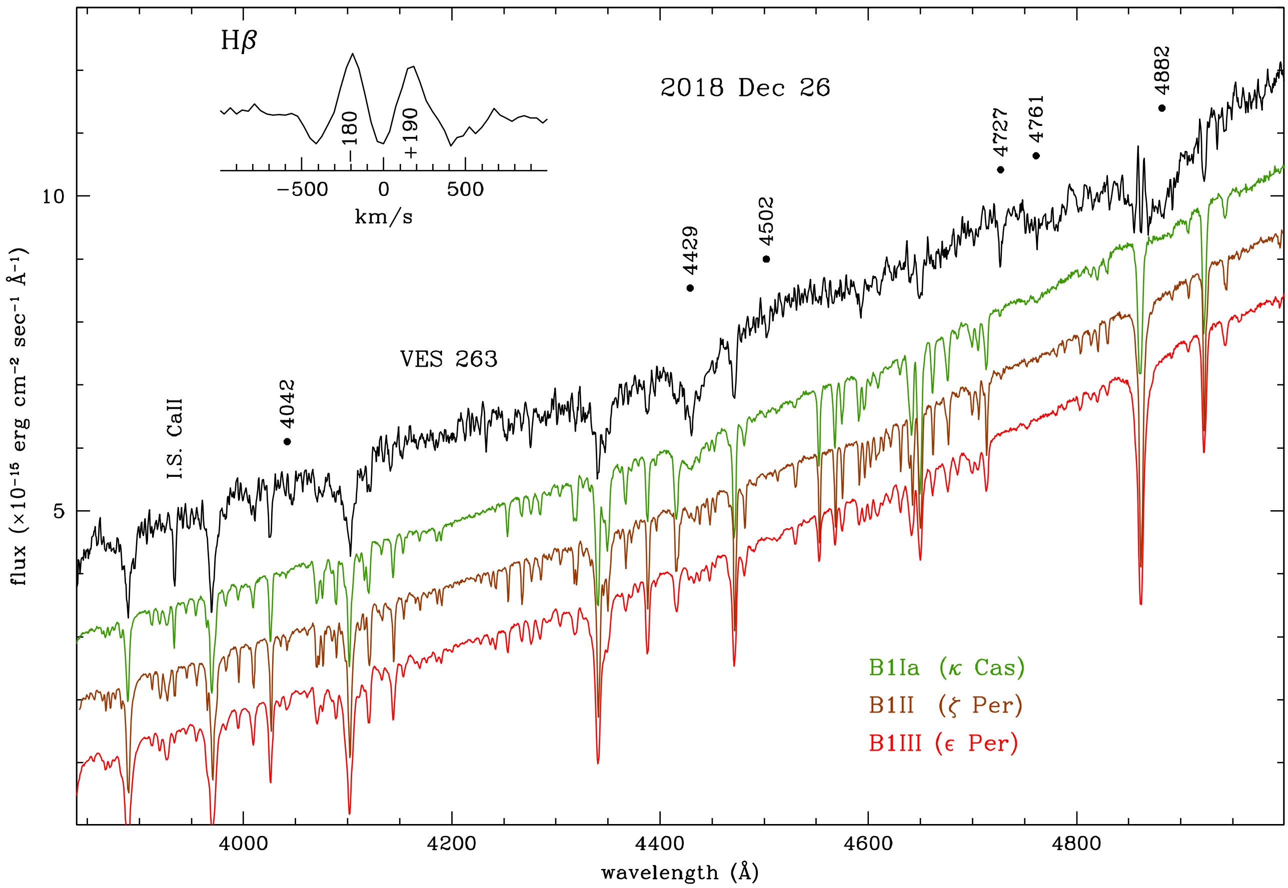

Figure 5. Medium-resolution spectrum (0.60 Å/pix) of VES 263 for 2018 December 26 compared to those of MKK standard stars observed with the same instrumental set-up. The standards have been scaled to the same flux and slope of VES 263 and have offsets applied for plot clarity. The inset shows the velocity profile of the Hβ double-peaked emission of VES 263. The dots mark the strongest diffuse interstellar bands.

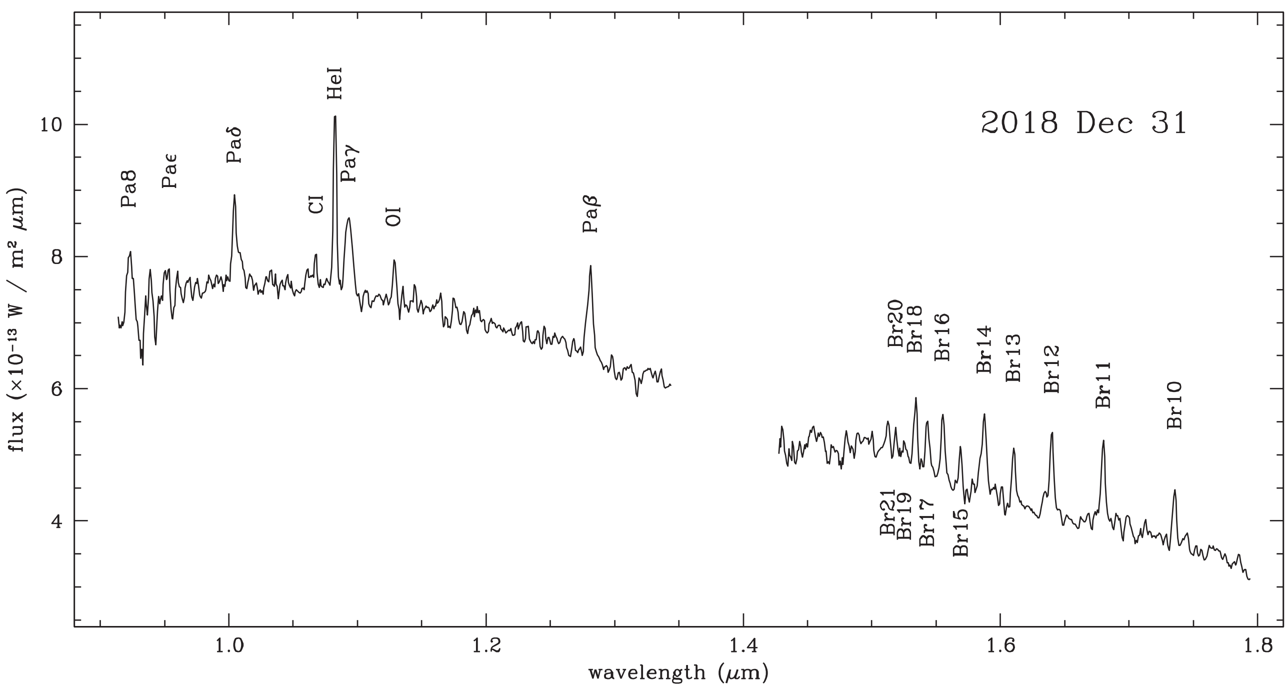

Figure 6. Near-IR spectrum of VES 263 for 2018 December 31 covering the *Y*-, *J*-, and *H*-band wavelength range. The strongest emission lines are identified.

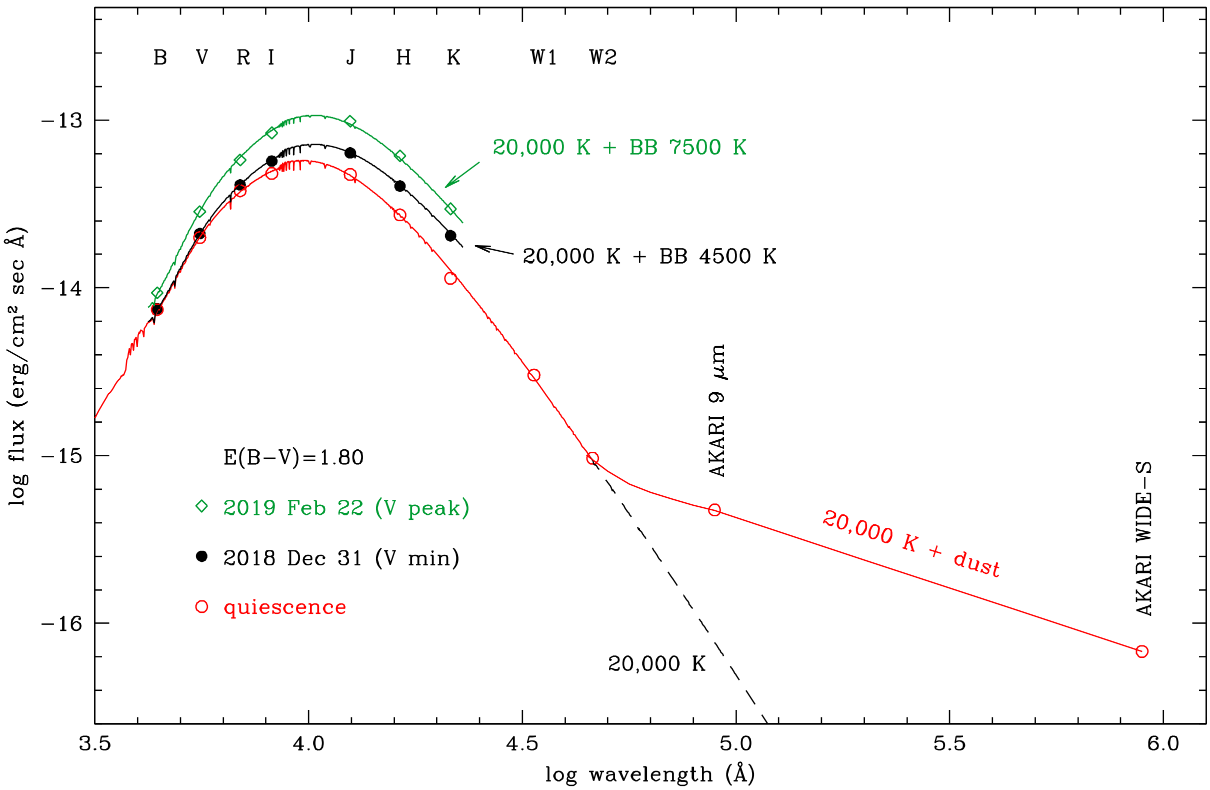

Figure 7. The spectral energy distribution of VES 263 at three distinct states (quiescence, and minimum, and peak brightness during the current eruption). The SED in quiescence is fitted with a synthetic spectrum for the B1II star and blackbody emission over 400–25 K for the dust. Blackbodies are added to the B1II star for the other epochs [all reddened by the same *E(B − V)* = 1.80].

such high densities, the Brackett hydrogen lines are expected to be optically thick (Hummer & Storey 1987; Storey & Hummer 1995).

4 THE SPECTRAL ENERGY DISTRIBUTION

The spectral energy distribution of VES 263 is presented in Fig. 7. Three epochs are considered: those of minimum and maximum in brightness during the current 2018–19 eruption, and the phase of preceding quiescence.

The spectral energy distribution (SED) in quiescence is built from 2009–2014 multi-epoch APASS optical photometry (reporting average values as $B = 14.93$, $V = 13.15$, $R = 12.11$, and $I = 11.22$), 2MASS JHK_s data for 1998 (Cutri et al. 2003), AKARI S9W, WIDE-S measurements for 2006–2007 (Ishihara et al. 2010; Alí-Lagoa et al. 2018), and AllWISE[1] W1, W2 data for 2010 (Cutri et al. 2013). Such data are obviously non-simultaneous, but since the object was in a quiescent state during this time, it should result in any significant difference.

The calibrations of the MK spectral types in terms of photospheric temperature, summarized by Tokunaga (2000) and Drilling & Landolt (2000), average to 20 000 K for B1 giant/supergiants. To fit the energy distribution for VES 263 in quiescence in Fig. 7, we have selected from the grid computed by Castelli & Kurucz (2003) the synthetic spectrum appropriate for a B1II star (parameters: $T_{\rm eff}$ = 20 000 K, [M/H] = 0.0, and $\log g = 3.0$), and adopted the Fitzpatrick (1999) extinction law for the standard $R_V = 3.1$ case. The excellent fit in Fig. 7 is obtained for $E(B-V) = 1.80$. A similar good fit and reddening would be obtained adopting a blackbody distribution for $T = 20\,000$ K. Both fitting with a synthetic spectrum and with a blackbody are not oversensitive to temperature: considering that the optical–IR is located on the Rayleigh–Jeans tail of the energy distribution for stars as hot as the B1II in VES 263, the actual temperature makes a small difference (fits with 19 000 or 21 000 K blackbodies or synthetic spectra would perform equally good in Fig. 7), and the shape of the observed SED is actually controlled by the reddening, with a change by $\Delta E(B-V) = \pm 0.05$ being readily appreciable.

The SED in quiescence shows a large excess over the 20 000 K photospheric emission for $\lambda \geq 6$ μm. The IR-excess in Fig. 7 is fitted by adding blackbody emission from dust distributed in temperature from 400 to 25 K. The presence of warm circumstellar dust is a distinctive feature of HAeBe stars (e.g. Stahler & Palla 2005). The luminosity radiated by such dust is $L_{\rm IR} \sim 12$ L$_\odot$. It was obtained by integrating the (unreddened) flux in excess of the 20 000 K photospheric synthetic spectrum in Fig. 7, and scaling it to the distance of VES 263 (Section 6).

The SEDs of VES 263 at minimum and peak brightness during the 2018–19 eruption are plotted in Fig. 7 using our simultaneous *BVRI* and *JHK* observations for 2018 December 31 and 2019 February 22, respectively. A good fit to the SED at minimum is obtained by adding a 4500 K blackbody to the synthetic spectrum for the B1II star. The SED at maximum is instead fitted by adding a 7500 K blackbody to the emission from the B1II central star [both 4500 and 7500 K blackbodies being reddened by the same $E(B-V)$ = 1.80 affecting the 20 000 K synthetic spectrum]. Such 4500 and

[1] We ignore AllWISE W3, W4 data because of conflicting results reported for PSF-fitting and aperture photometry measurements, and their large scatter depending on the radius of aperture.

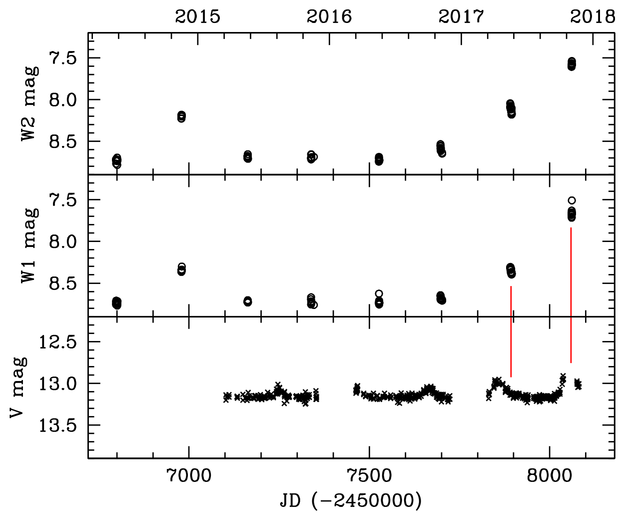

Figure 8. Comparison between NeoWISE data and *V*-band photometry of VES 263. The lines are meant to guide the eye.

7500 K blackbodies have, respectively, λ-integrated luminosities of 120 and 860 $L_\odot$. This fitting exercise shows that the brightness and colours during the eruption of VES 263 are governed by the presence and variability of a source both cooler and separate/additional to the central B1II star, which we identify with the circumstellar disc (see Section 8 below) that is a typical feature of pre-main-sequence objects (Stahler & Palla 2005). The surface temperature of a disc obviously depends on the distance from the central star, and therefore the 4500 and 7500 K values found above are to be interpreted as averages weighted over the respective surfaces emitting at *BVRI* and *JHK* wavelengths.

It is worth noticing that the minor brightenings visible in the pre-eruption light curve of Fig. 2 are also linked to the variable presence of a source much cooler than the stellar photosphere (i.e. the disc). This can be easily inferred from Fig. 8, where the NeoWISE data (Mainzer et al. 2011, 2014) available for VES 263 are plotted in phase with the *V*-band light curve. It is evident how (1) during quiescence the NeoWISE *W*1 and *W*2 data (Nugent et al. 2015) stay flat and close to the AllWISE $W1 = 8.58$ and $W2 = 8.50$ mag values characterizing the quiescent SED of Fig. 7, and (2) any minimal brightening visible in the *V* band reverberates into a much larger increase at NeoWISE *W*1 and *W*2 wavelengths. The AllWISE catalogue combines observations from the 2009–2010 cryogenic and post-cryogenic survey phases of the NASA Wide-field Infrared Survey Explorer (WISE), and NeoWISE refers to the data the satellite is collecting since it has been brought out of hibernation and resumed observation in 2014.

5 ASTROMETRIC MEMBERSHIP TO THE CYG OB2 ASSOCIATION

Analysis of *Gaia* astrometry supports VES 263 being a member of the Cyg OB2 association. To this aim, we started by acquiring a list of hot OB stars in this association compiled by Wright, Drew & Mohr-Smith (2015) and in an extended region around the densest part of the association by CP12 and Berlanas et al. (2018). As their membership designation is historically mainly attributed by overdensity of spectroscopically confirmed OB stars in that region (Ivanov 1996), we first queried *Gaia* DR2 data (Gaia Collaboration 2018) in a cone with the radius of 1° centred at $\alpha = 308.163^\circ$

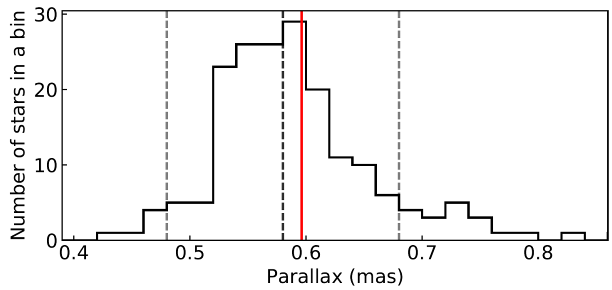

Figure 9. Distribution of *Gaia* DR2 parallax measurements of confirmed members of the Cyg OB2 association. The parallax of VES 263 is marked with the red vertical solid line. The black vertical dotted lines indicate our parallax selection, centred at 0.58 mas, that was used to study the proper motion of the association.

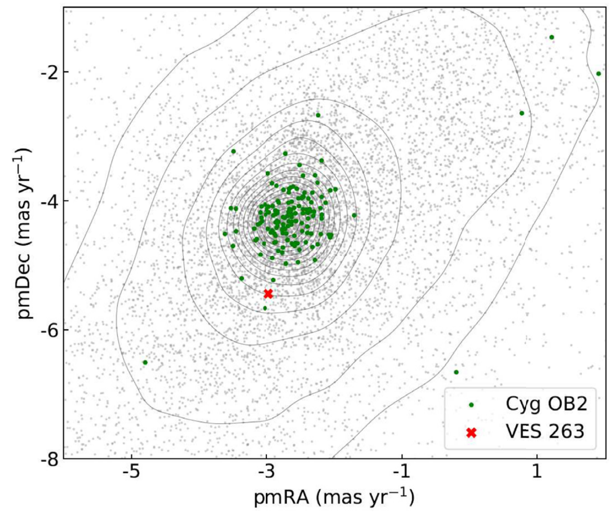

Figure 10. Distribution of selected stars in proper motion space, with indicated association members and VES 263. The density profile, shown as equidistant contours, was created by summing 2D Gaussian probability density function (PDF) of all stars. PDFs were defined by stellar proper motion and its reported uncertainty.

$\delta = 41.299^\circ$ and matched the *Gaia* observations with previously determined members. Already confirmed by Berlanas et al. (2019), the members are concentrated around parallax ∼0.58 mas with a possible extension to closer distances. VES 263, marked with a solid vertical line in Fig. 9, is located close to the peak of that distribution.

Having more than 800 000 stars, which could smear out over-densities of few hundreds of stars in the proper motion space, we limited our selection to stars with a parallax measurement between 0.48 and 0.68 mas (also indicated in Fig. 9). This selection resulted in 11 561 stars of which 153 are members of the association, together plotted in Fig. 10. The same figure shows overdensity of stars with the same proper motion as known Cyg OB2 members. If we move our selection to higher/lower parallax values, the overdensity disappears. VES 263 falls on the outskirts of this peak, where the density of stars in proper motion space starts to increase. Disregarding the clear velocity outliers, which might not be part of the association, VES 263 has a velocity consistent with other members. As the OB associations are proven not to be bound (Mel’nik & Dambis 2017; Wright 2018) and have larger physical sizes than open clusters with considerable small-scale kinematics substructure (Wright 2018), a greater velocity scatter is expected for

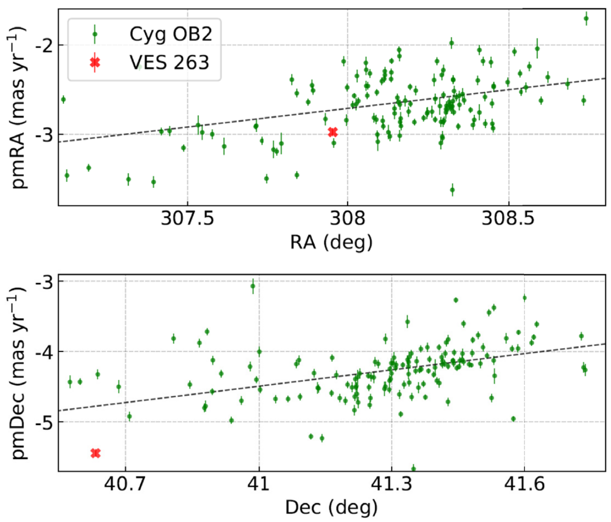

Figure 11. Distribution of proper motion and sky location of the Cyg OB2 members and VES 263 in the right ascension (*top*) and declination (*bottom*) planes.

them. As VES 263 is not located in the main part of the association, but in its extended region, its velocity vector might indicate radial expansion. The plots in Fig. 11 show dependency of members' proper motion on their position in the sky. Both the plots show some trends, where VES 263 is consistent with the scatter along the fitted line and therefore membership to Cyg OB2.

From fitting to isochrones, Wright et al. (2015) concluded that the majority of star formation in Cyg OB2 occurred more or less continuously between 1 and 7 Myr ago, which should then bracket the age of VES 263. At an estimated total mass of $\sim$16 500 M$_\odot$, Cyg OB2 is one of the most massive groups of young stars known in our Galaxy.

6 DISTANCE AND INTERSTELLAR REDDENING

The *Gaia* DR2 parallax for VES 263 is 0.5962 mas, with an error of just $\pm$0.0253 (4 per cent) that allows a safe direct inversion (Gaia Collaboration 2018) to derive the distance as $\sim$1.68 $\pm$ 0.07 kpc. At a Galactic latitude of only +0.60 deg, the sightline accumulates a lot of interstellar reddening upon reaching VES 263, as already clear from the SED fitting of the previous section requiring $E(B-V) = 1.80 \pm 0.05$.

There are several 3D maps of interstellar extinction that may be employed to derive estimates of the reddening affecting VES 263. STILISM by Lallement et al. (2014) and Capitanio et al. (2017) provides $E(B-V) = 1.98 \pm 0.25$, and the 3D Pan-STARRS1 map by Green et al. (2018) returns $E(B-V) = 2.06 \pm 0.21$. An appreciable lower error is associated with the IPHAS 3D map by Sale et al. (2014) giving an extinction $A_V = 6.19$, with lower and upper limits at $A_V = 5.85$ and 6.55, respectively, combining IPHAS and *Gaia* uncertainties. For the $R_V = 3.1$ extinction law, using the quadratic expression of Fiorucci & Munari (2003) for early B-type stars suffering from high reddening, this translates to $E(B-V) = 1.92$ with formal lower and upper limits of $E(B-V) = 1.82$ and 2.03, respectively.

At such high reddening, the interstellar Na I lines are too strong (core saturated) in our Echelle spectra of VES 263 to allow using them to derive the reddening, as illustrated in Fig. 12. Interstellar K I lines are however still far from saturation. The equivalent width (EW) 0.410 $\pm$ 0.006 Å that we have measured for K I 7699 Å on our Echelle and medium-resolution spectra (cf. Fig. 12) translates into $E(B-V) = 1.76 \pm 0.03$ following the calibration by Munari & Zwitter (1997).

The diffuse interstellar bands (DIBs) do present a general trend to get stronger with increasing reddening (e.g. Jenniskens & Desert 1994), but the correlation is far from being a tight or unique one. Our Echelle spectra of VES 263 have recorded a rich sample of DIBs, a few being shown in Fig. 12. Two sightline categories, named ζ and σ, have been described by Krelowski et al. (1992) and Krelowski & Sneden (1994), which correspond to *UV-shielded* and *non-shielded* sightlines, probing cloud cores and external regions, respectively. Vos et al. (2011) show that there are fundamental differences between the two groups in correlations between DIBs, reddening, and gas. The two sightline categories are named after those towards ζ Oph and σ Sco. Kos & Zwitter (2013) found that DIBs at 5705, 5780, 6196, 6202, and 6270 Å do not show much difference between ζ and σ sightlines, while DIBs at 4964, 5797, 5850, 6090, 6379, and 6660 Å have distinctly different relations for ζ and σ sightlines between their EW and $E(B-V)$ reddening. The ratio of the EW of DIBs 5780 and 5797 allows us to distinguish between the two types of sightlines: an $\mathrm{EW}_{5797}/\mathrm{EW}_{5780} > 0.3$ corresponds to ζ category, and conversely an $\mathrm{EW}_{5797}/\mathrm{EW}_{5780} < 0.3$ to σ category. The DIBs at 5780 and 5797 Å in our Echelle spectra of VES 263 are shown in Fig. 12. Their EWs are 0.755 and 0.330 Å, respectively, corresponding to ζ-type sightline categories. In Table 5 we report our measurement of the EW of the DIBs best visible in our Echelle spectra of VES 263, and the corresponding reddening $E(B-V)$ derived by applying the ζ-type calibration given by Kos & Zwitter (2013). Such reddenings tightly cluster around two distinct values, $E(B-V) = 1.21 \pm 0.02$ and 1.42 ± 0.03. Such values are mutually incompatible and also far too small compared to all other indicators summarized in Table 5. Other E.W./$E(B-V)$ calibrations for DIBs (e.g. Munari 2014) result in values similar to those of Table 5, and therefore we conclude that DIBs along the sightline to VES 263 do not conform to published reddening relations calibrated over large portions of the sky.

The three most accurate reddening determinations among those summarized in Table 5 come from K I 7699, SED fitting, and IPHAS 3D map, for an average value of $E(B-V) = 1.80 \pm 0.05$ that we will adopt in the rest of this paper.

7 ABSOLUTE MAGNITUDE AND THE HR DIAGRAM

From the *Gaia* DR2 parallax, $E(B-V) = 1.80$ reddening and APASS $V = 13.15$, the absolute magnitude of VES 263 in quiescence is $M_V = -3.75$ mag. This is equivalent to a bolometric magnitude $M_{\mathrm{bol}} = -5.64$ mag adopting from Flower (1996) a bolometric correction B.C. = -1.89 for giants/supergiants with $T_{\mathrm{eff}} = 20\,000$ K, and $M_{\mathrm{bol}}^{\mathrm{Sun}} = +4.74$ (Bessell, Castelli & Plez 1998; Torres 2010). The corresponding luminosity is $L = 14\,000$ L$_\odot$, which is close to $L = 12\,000$ L$_\odot$ as obtained by direct flux integration of the (unreddened) synthetic $T_{\mathrm{eff}} = 20\,000$ K spectrum in Fig. 7.

The position on the HR diagram of HAeBe stars as catalogued by Vioque et al. (2018) is shown in Fig. 13. The position and error bars for VES 263 correspond to $L = 13\,000 \pm 3000$ L$_\odot$ and T_{eff}

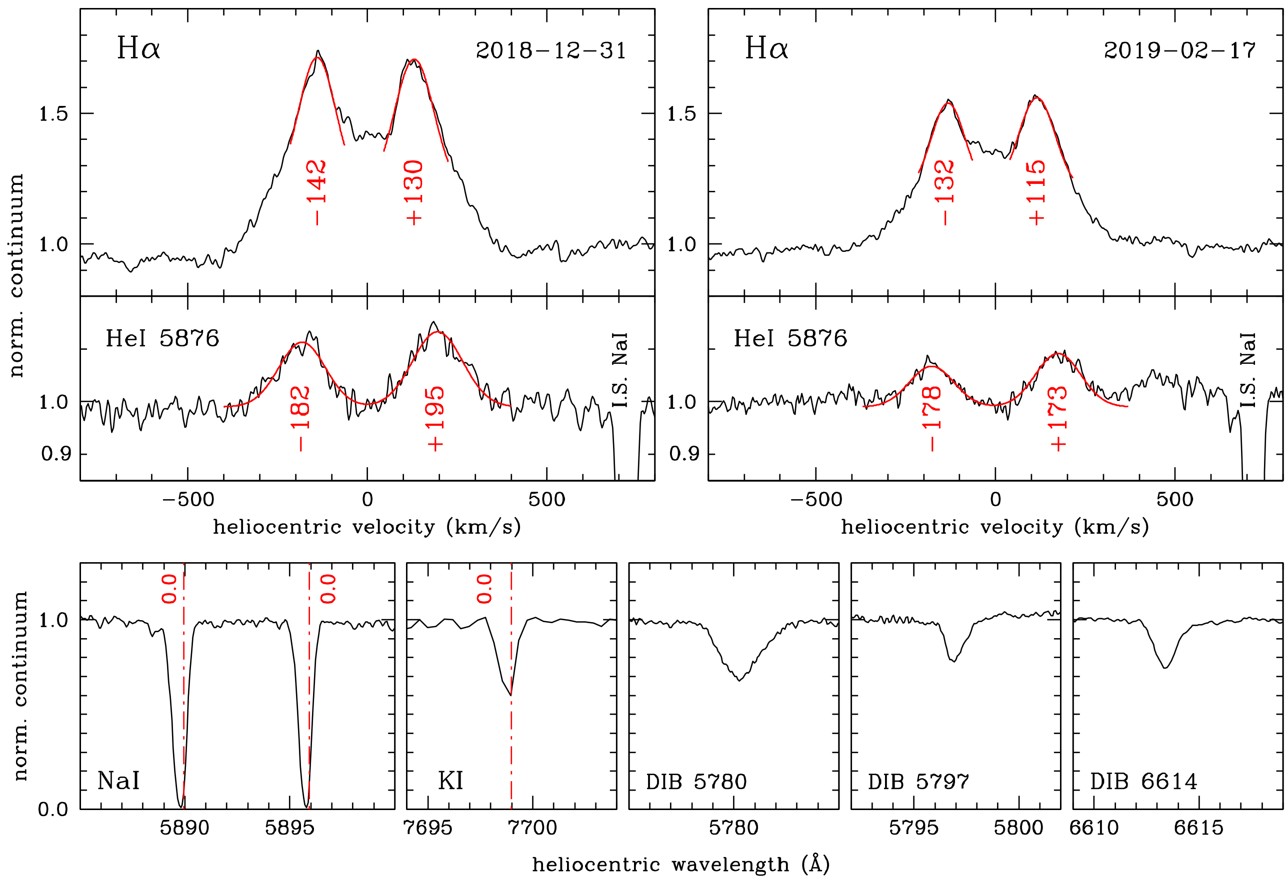

Figure 12. *Top*: Gaussian fitting to the double-peaked line profiles of Hα and He I 5876 for minimum (left) and maximum (right) brightness during the 2018–19 eruption. *Bottom*: interstellar lines and DIBs as recorded on the Asiago Echelle spectra. The dash–dotted lines mark null heliocentric radial velocity.

Table 5. Summary of results from reddening indicators. E.W. is the equivalent width of the interstellar spectral feature and $E(B-V)$ the corresponding reddening as derived from the published relations discussed in Section 6.

	E.W. (Å)	Err	$E(B-V)$	Err
DIB 5705	0.1372	0.0036	1.23	0.03
DIB 5797	0.2264	0.0014	1.23	0.01
DIB 5850	0.1018	0.0015	1.20	0.02
DIB 6379	0.1389	0.0022	1.18	0.02
		Mean:	1.21	0.02
DIB 5780	0.7592	0.0081	1.40	0.02
DIB 6196	0.0787	0.0070	1.41	0.11
DIB 6270	0.1527	0.0067	1.44	0.06
DIB 6614	0.3511	0.0081	1.43	0.03
		Mean:	1.42	0.03
Pan-STARRS 1	–	–	2.06	0.21
Stilism	–	–	1.98	0.25
KI 7699	0.4096	0.006	1.76	0.03
B1II SED	–	–	1.80	0.05
IPHAS 3D	–	–	1.92	0.12
	Adopted:		1.80	0.05

$= 20\,000 \pm 2000$ K. The corresponding blackbody radius would be 9.5 ± 1.2 R$_\odot$. In the same figure, we have plotted the pre-main-sequence tracks for three values of the mass from Bressan et al. (2012), leading to an estimate of ≈12 M$_\odot$ for VES 263.

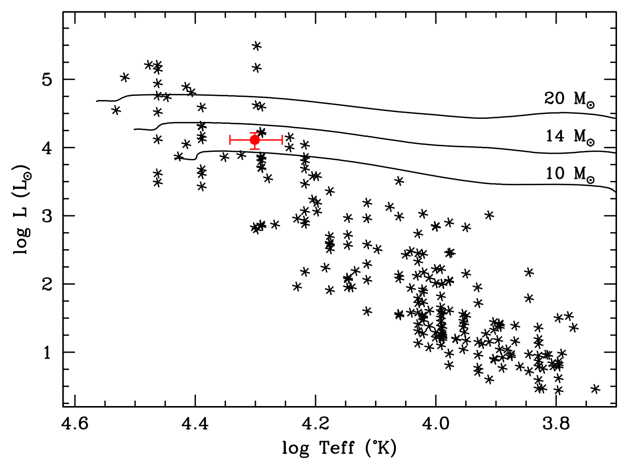

Figure 13. The position of VES 263 on the HR diagram. The asterisks mark data for the HAeBe stars in the compilation by Vioque et al. (2018). The lines are pre-main-sequence evolutionary tracks from Bressan et al. (2012).

8 THE ACCRETION DISC

8.1 Evidence from emission-line profiles

The emission profiles for Hα and He I 5876 in VES 263 at the time of maximum and minimum brightness during the 2018–19 eruption are plotted in Fig. 12. Such double-peaked profiles are typical of circumstellar discs (Horne & Marsh 1986). The origin

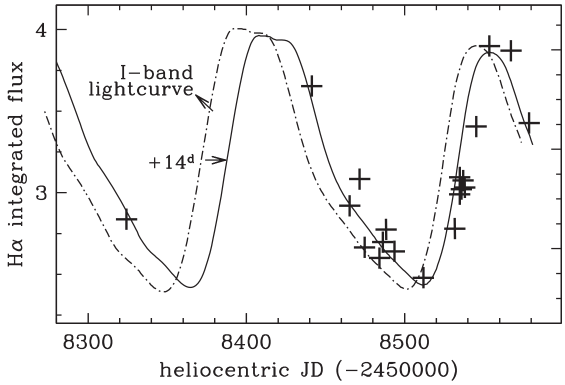

Figure 14. Evolution with time of the integrated flux of Hα emission line of VES 263, from data in Table 2. The dot–dashed line is the *I*-band light curve from Fig. 1; the same shifted by 14 d is plotted as the continuous line.

in a disc is reinforced noting that the peaks of He I lines have a larger velocity separation than Hα. The excitation potential for He I 5876 is ∼23 eV, twice larger than the ∼12 eV for Hα, and population of the upper level for He I 5876 requires hotter and denser regions compared to Hα, which means an inner disc radius and therefore a faster Keplerian rotation. The ratio of velocity separation of the double-peaked Hα:He I 5876 profiles goes like 1.0:1.4 for VES 263, which quite favourably compares with the average value 1.0:1.5 we have measured for a sample of quiescent cataclysmic variables (CVs) we have observed over the years with the same Asiago Echelle spectrograph used to observe VES 263. In CVs, the emission lines are well known to form in the accretion disc around the central white dwarf (e.g. Warner 1995).

From line fitting in Fig. 12, the projected rotational velocity of the disc at the location of Hα formation is $v\sin i \sim 130$ km s^{-1}. Assuming a pure Keplerian rotation for the disc and adopting from the previous section 12 M$_\odot$ and 9.5 ± 1.2 R$_\odot$ for the central star, the Hα forms at ≈14 stellar radii for an inclination of the disc $i = 90^\circ$ and ≈7 stellar radii for $i = 45^\circ$.

In addition to the SED distributions in Fig. 7, the disc as the agent responsible for the variability observed in 2018–19 is also supported by the evolution with time of the integrated flux of Hα, which is listed in Table 2 and plotted in Fig. 14. The Hα behaviour in Fig. 14 matches exactly the light curve of VES 263. For the latter, we selected the *I*-band brightness because its effective wavelength is the closest to the peak of the energy distribution of VES 263 (cf. Fig. 7). The $\Delta I = 0.50$ mag amplitude of the light curve translates into a change of the photometric flux by 58 per cent, which is the same as the 54 per cent change in the integrated flux of Hα as listed in Table 2.

A noteworthy feature in Fig. 14 is the ∼14 d shift between Hα and the *I* band. The brightness of the disc is proportional to the mass flow through it (Ichikawa & Osaki 1992). Similarly, the integrated flux of Hα traces the mass flow through the inner regions of the disc where the temperature is high enough to excite the emission from the line. The ∼14 d delay appears therefore to be the average time required for mass to migrate from the outer regions of the disc where the bulk of the emission in the *I*-band originates to the inner regions where the temperature is hot enough to excite emission from Hα.

A final remark on the disc is offered by Fig. 12. Close to minimum brightness (2018 December spectrum) the velocity separation of the double-peaked line profiles is larger than at maximum brightness (2019 February spectrum). A higher brightness corresponds to a

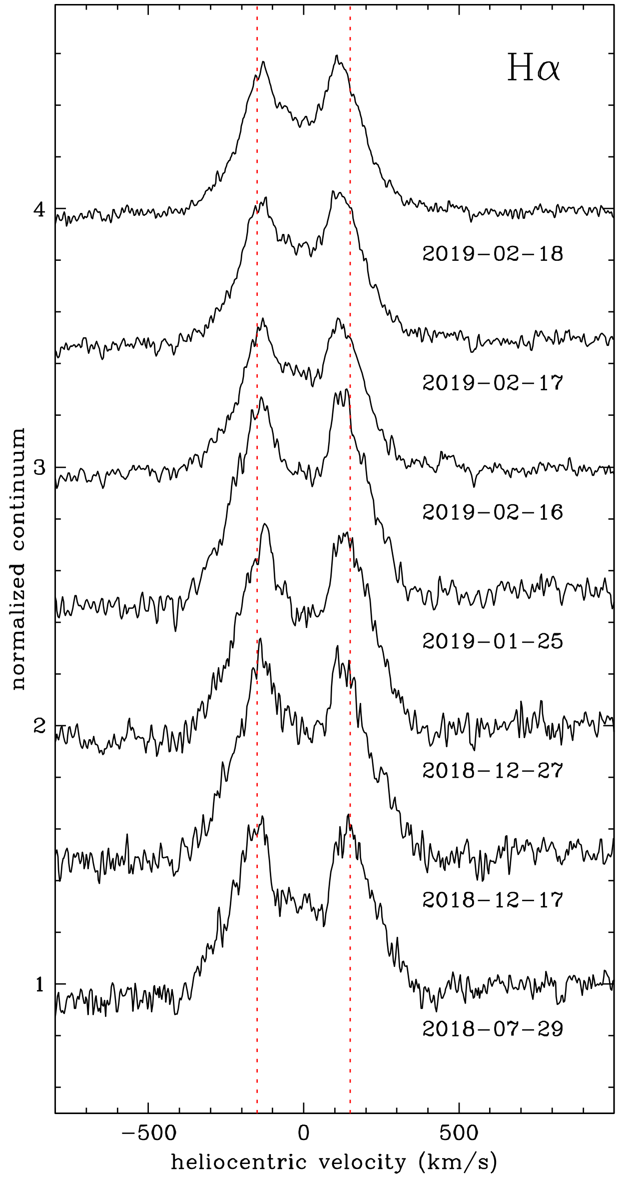

Figure 15. Comparison of the Hα emission profile of VES 263 as observed at different epochs with the Asiago 1.82m +Echelle spectrograph (adjacent continuum normalized to 1.0). The lines at −150 and +150 km s^{-1} are plotted to guide the eye.

larger mass flow through the disc, and therefore a given temperature is reached at an outer radius (given the classical $T_{\rm eff} \propto M_{\rm acc}^{1/4}$ dependence). The temperature required to excite emission from Hα is then reached at a greater distance from the central star, resulting in a lower Keplerian velocity and consequently a reduced velocity separation of the double-peaked line profile (similarly for He I 5876). Precisely what is seen in Fig. 12.

8.2 Looking for orbital motion

The high-resolution Echelle spectroscopic observations of VES 263 listed in Table 2 cover a time interval of about 200 d. Photospheric absorption lines are veiled by featureless continuum emission by the disc, leaving only the Hα emission line to derive the radial velocity. A sample of the recorded Hα profiles is presented in Fig. 15.

Many massive stars are found in binary systems, as it is the case for the majority of O- and B-type stars in open clusters and OB associations (e.g. Boeche et al. 2004), with mass ratios closer to $q \sim 1$ than less massive binaries. Their orbital periods can be as short as 1–2 d with consequently orbital velocities of hundreds of km s^{-1}. The line photocentre in Fig. 15 is stable around the average value of $RV_\odot = -4.1 \pm 0.9$ km s^{-1}. The dispersion of measurement ($\sigma = 2.5$ km s^{-1}) is similar to the dispersion of intra-night individual spectra, suggesting minimal or null change in radial velocity during the monitored 200 d. This leads to basically three different explanations: (1) the B1II star is single, or any companion is far less massive ($q \ll 1$), (2) the orbital period is much longer than the sampled 200 d, or (3) the orbital inclination is very low (face-on orientation). The latter explanation is the less probable, because it is reasonable to assume that in a binary the circumstellar disc lies close to the orbital plane, and the disc in VES 263 has a considerable inclination given the large velocity separation of the peaks in the emission-line profiles (Fig. 12). Alternatives 1 and 2 could either be true, as their combination. To further investigate them, we plan to continue gathering high-resolution spectra of VES 263 in the future.

In addition to keeping their photocentre stable, the line profiles in Fig. 15 do not change their shape other than reducing the velocity separation in response to changes in the mass flow through the disc. This indicates that over the 200 d of monitoring the inner regions of the disc where Hα forms remained circular and symmetric, excluding precession of an asymmetric shape for the disc.

8.3 Mass accretion rate

Mass accretion ($M_{\rm acc}$) and accretion luminosity ($L_{\rm acc}$) are related by

$$L_{\rm acc} = G\frac{M_* M_{\rm acc}}{R_*}\,, \tag{1}$$

where M_* and R_* are the mass and radius of the accreting object, respectively. This can be used to obtain an order-of-magnitude estimate of the mass flow rate through the disc of VES 263 and on to its central star.

The SED of VES 263 at maximum and minimum brightness during the current 2018–19 eruption is characterized by excess radiation at optical and near-IR wavelengths that, when fitted with blackbodies and their emission integrated over the whole wavelength range, provides luminosities of 860 and 120 L$_\odot$, respectively (cf. Fig. 7 and Section 4). The corresponding mass accretion rates would be 1.12×10^{-5} and 1.43×10^{-6} M$_\odot$ yr^{-1}. They are however lower limits to the actual value of $M_{\rm acc}$, because the fit with blackbodies of $T_{\rm eff} = 7500$ and 4500 K misses the emission from the inner and hotter regions of the disc able to sustain the formation of Balmer and He I emission lines. To access them, it would be essential to gather satellite observations in the ultraviolet, difficult to obtain in view of the very large extinction affecting VES 263 (of the order of 15 mag at 2000 Å).

To test the hypothesis that the accretion luminosities derived in the previous paragraph are lower limits, we may estimate $L_{\rm acc}$ from the reddening-corrected observed flux ($F_{\rm line}$) of emission lines, following a common practice for pre-main-sequence objects.The isotropically radiated luminosity $L_{\rm line}$ in the given line is related to distance d through

$$L_{\rm line} = 4\pi d^2 F_{\rm line}\,. \tag{2}$$

The transformation of $L_{\rm line}$ into $L_{\rm acc}$ is usually obtained by power-law relations of the type

$$\log\left(\frac{L_{\rm acc}}{\rm L_\odot}\right) = A_{\rm line} + B_{\rm line} \times \log\left(\frac{L_{\rm line}}{\rm L_\odot}\right) \tag{3}$$

with calibrations of $A_{\rm line}$, $B_{\rm line}$ coefficients existing for many emission lines. Integrating the flux of emission lines visible in the near-IR spectrum of Fig. 6 and adopting their $A_{\rm line}$, $B_{\rm line}$ coefficients from Fairlamb et al. (2017) lead to accretion luminosities ranging from 200 to 1300 L$_\odot$, with a median value of 900 L$_\odot$. This confirms as a lower limit the 120 L$_\odot$ accretion luminosity derived above from integration of SED for the same date (2018 December 31), the time of minimum during the current 2018–19 eruption. It would have been interesting to repeat the exercise with a similar near-IR spectrum taken during a maximum in the current 2018–19 eruption, but unfortunately we have none. We do have however in Table 2 an extended series of flux measurements for the Hα emission line. Adopting the corresponding $A_{\rm line}$, $B_{\rm line}$ coefficients from Mendigutía et al. (2011), the derived accretion luminosities range from 280 to 450 L$_\odot$. The amount of reddening correction to Hα is however vastly larger than for the near-IR emission lines, and uncertainties on $E(B-V)$ could easily account for part of the 2× difference in their respective $L_{\rm acc}$.

The accretion luminosity $L_{\rm acc}$ has also been found to correlate with the luminosity of the central star $L_\star$. The analysis of existing data by Mendigutía et al. (2015) shows that for HAeBe the accretion luminosity ranges from $L_{\rm acc} \sim L_\star$ to $0.01\,L_\star$. VES 263 follows this rule with – from the data above – $L_{\rm acc} \sim 0.07 \times L_\star$ at minimum and $L_{\rm acc} \sim 0.5 \times L_\star$ at maximum of the current 2018–19 eruption.

Finally, it appears worth noticing that the recent calibration by Arun et al. (2019) of $M_{\rm acc}$ as a function of the mass of the central star in HAeBe objects predicts $M_{\rm acc} \approx 3.3 \times 10^{-5}$ M$_\odot$ yr^{-1} for a 12 M$_\odot$ star as in VES 263. This well compares with the lower limit $M_{\rm acc} \geq 1.1 \times 10^{-5}$ M$_\odot$ yr^{-1} estimated in this section for the accretion rate at the peak of the present VES 263 eruption.

8.4 Wind and jets

The low-resolution spectra listed in Table 2 show a low-level variability in the immediate vicinity of Hα emission line. They are compared in Fig. 16. To avoid confusion with the many DIBs present in the region, the principal ones are identified in the top panel of the figure. Three numbers are given for each DIB, namely the FWHM (in Å), the EW (in Å, scaled to that of DIB 6614), and the wavelength of the photocentre (in Å), averaging among the values reported by Jenniskens & Desert (1994) in their surveys of DIBs towards several hot stars. Fig. 16 shows that indeed the dispersion of individual spectra is larger in the immediate vicinity of Hα.

A variable *hump* is present in emission to the red of Hα, at a bulk velocity of ≈+700 km s^{-1}. Symmetrically placed at a bulk velocity of ≈−700 km s^{-1} there is a variable absorption, or as an alternative a variable second emission hump. To distinguish between these two alternatives for the blue feature is not easy in view of the limited spectral resolution and S/N of the spectra in Fig. 16. To complicate the matter is the deep depression of the stellar continuum caused by the nearby very strong DIB 6532. Devoted observations, at higher S/N and greater spectral dispersion, are required to properly address the issue, which we plan to perform in the future. These features are relatively minor, carrying a flux ∼1/10 of that of the main Hα line. They are barely at the threshold of detection in Echelle observations, being lost in the strong curvature imposed by the instrumental blaze function at the centre of the order, where Hα is situated.

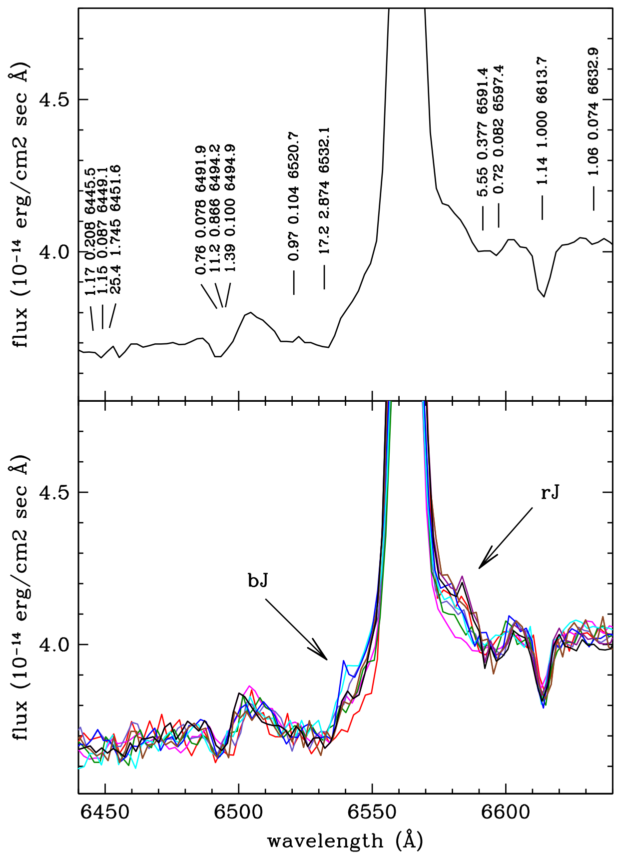

Figure 16. *Top panel:* average around Hα of the low-resolution spectra of VES 263. The strongest DIBs in the compilation by Jenniskens & Desert (1994) are marked (see Section 8.4 for associated numbers). *Bottom panel:* the individual spectra making up the above average are plotted individually (after matching their median value). The arrows point to regions at ≈ -700 and $+700$ km s^{-1} where the dispersion is larger (see section 7.4).

We propose the features at $+700$ and -700 km s^{-1} to be the signature of possible bipolar jet ejection from the central regions of the accretion disc surrounding the central star. That at -700 km s^{-1} could appear in absorption instead of emission if seen projected on to the central B1II star or the brightest inner regions of the disc. The escape velocity from the central star is $\sim$700 km s^{-1} (assuming $R = 9.5$ R$_{\odot}$ and $M = 12$ M$_{\odot}$). The similarity of the jet velocity and the escape velocity is a general property of all objects known to possess collimated mass outflows (Livio 1997). Bipolar jets have been observed in many HAeBes (Stahler & Palla 2005), sometimes extending to such great distances from the central star to be easily resolved spatially by ground-based observations (e.g. Corcoran & Ray 1998; Grady et al. 2004; Melnikov et al. 2008; Günther, Schneider & Li 2013).

9 CONCLUSIONS

The observational evidence discussed in previous sections proves the variable presence of a massive accretion disc in VES 263. The SED in Fig. 7 shows how the contribution of such a disc was negligible when the object was in quiescence, and becomes dominant at redder wavelengths during the current 2018–19 eruption. Furthermore, the strict parallel behaviour between disc brightness and integrated Hα flux shown in Fig. 14 proves how the ups and downs in the light curve are correlated to the variable mass flow through the disc.

What causes such a variability in the mass being fed to the disc is unknown, and its investigation is beyond the scope of this paper. It is however intriguing to note from Figs 1 and 2 how the photometric activity and mean brightness have been increasing on the average during the last few years, signalling a gradual resumption of mass feeding and flow through the disc. This behaviour seems parallel to the slow and contrasting rise ($\sim$8 yr) from quiescence to peak brightness at the time of the large eruption of the 1950's, illustrated in Fig. 3. It is tempting to argue that the 1950's eruption was caused by a similar resumption of the accretion disc as we are witnessing now. If the current event should turn into a replica of the eruption of the 1950's, then we are at present only just half-way to its peak brightness.

VES 263 is clearly worth a continuing detailed, multiwavelength monitoring over the coming years, as well as a dedicated effort to locate further information about its colourful past history.

ACKNOWLEDGEMENTS

We are grateful to the anonymous referee for valuable comments that helped to improve the paper. We acknowledge Jonathan Grindlay and Edward Los of Harvard College Observatory for their permission to use DASCH data on VES 263 prior to inclusion in public DR6 scheduled for 2019. RJS thanks the team of Sonneberg Observatory and 4pi Systeme company for hospitality and Peter Kroll and Eberhard Splittgerber for help and permission to use the historical plate archive. The research work at the Physical Research Laboratory is funded by the Department of Space, Government of India. SYS is supported by Grant VEGA No. 2/0008/17 and Development Program from M.V. Lomonosov Moscow State University ('Physics of stars, relativistic objects and galaxies'). KČ acknowledges financial support of the Slovenian Research Agency (research core funding No. P1-0188 and project N1-0040). RJŠ is supported by University of Rijeka under the project number uniri-prirod-18-3. The observations presented in this paper have been collected in part with ANS Collaboration telescopes, the Galileo 1.22 m telescope of the University of Padova, and the INAF Copernico 1.82 m and Schmidt 67/92 cm telescopes.

REFERENCES

Alí-Lagoa V., Müller T. G., Usui F., Hasegawa S., 2018, A&A, 612, A85
Arun R., Mathew B., Manoj P., Ujjwal K., Kartha S. S., Viswanath G., Narang M., Paul K. T., 2019, AJ, 157, 159
Banerjee D. P. K., Ashok N. M., 2012, Bull. Astron. Soc. India, 40, 243
Berlanas S. R., Herrero A., Comerón F., Pasquali A., Bertelli Motta C., Sota A., 2018, A&A, 612, A50
Berlanas S. R., Wright N. J., Herrero A., Drew J. E., Lennon D. J., 2019, MNRAS, 484, 1838
Bessell M. S., Castelli F., Plez B., 1998, A&A, 333, 231
Boeche C., Munari U., Tomasella L., Barbon R., 2004, A&A, 415, 145
Bressan A., Marigo P., Girardi L., Salasnich B., Dal Cero C., Rubele S., Nanni A., 2012, MNRAS, 427, 127
Capitanio L., Lallement R., Vergely J. L., Elyajouri M., Monreal-Ibero A., 2017, A&A, 606, A65
Castelli F., Kurucz R. L., 2003, in Piskunov N., Weiss W. W., Gray D. F., eds, Proc. IAU Symp. 210, Modelling of Stellar Atmospheres, Poster Contributions. Kluwer, Dordrecht, p. A20
Comerón F., Pasquali A., 2012, A&A, 543, A101(CP12)
Corcoran M., Ray T. P., 1998, A&A, 336, 535
Cutri R. M. et al., 2003, yCat, 2246

Cutri R. M. et al., 2013, yCat, 2328
Downes R. A., Keyes C. D., 1988, AJ, 96, 777
Drilling J. S., Landolt A. U., 2000, in Cox A. N., ed., Allen's Astrophysical Quantities, 4th edn. AIP Press, New York, p. 381
Fairlamb J. R., Oudmaijer R. D., Mendigutia I., Ilee J. D., van den Ancker M. E., 2017, MNRAS, 464, 4721
Fiorucci M., Munari U., 2003, A&A, 401, 781
Fitzpatrick E. L., 1999, PASP, 111, 63
Flower P. J., 1996, ApJ, 469, 355
Gaia Collaboration, 2018, A&A, 616, A1
Grady C. A. et al., 2004, in Holt S. S., Deming D., eds, AIP Conf. Proc. Vol. 713, The Search For Other Worlds. Am. Inst. Phys., New York, p. 47
Green G. M. et al., 2018, MNRAS, 478, 651
Grindlay J., Tang S., Los E., Servillat M., 2012, in Griffin E., Hanisch R., Seaman R., eds, Proc. IAU Symp. 285, New Horizons in Time-Domain Astronomy. Kluwer, Dordrecht, p. 29
Günther H. M., Schneider P. C., Li Z.-Y., 2013, A&A, 552, A142
Henden A., Munari U., 2014, Contrib. Astron. Obs. Skalnaté Pleso, 43, 518
Herbig G. H., 1960, ApJS, 4, 337
Horne K., Marsh T. R., 1986, MNRAS, 218, 761
Hummer D. G., Storey P. J., 1987, MNRAS, 224, 801
Ichikawa S., Osaki Y., 1992, PASJ, 44, 15
Ishihara D. et al., 2010, A&A, 514, A1
Ivanov G. R., 1996, Astron. Astrophys. Trans., 9, 305
Jenniskens P., Desert F.-X., 1994, A&AS, 106, 39
Kochanek C. S. et al., 2017, PASP, 129, 104502
Kohoutek L., Wehmeyer R., 1997, AAHam, 11, 1
Kohoutek L., Wehmeyer R., 1999, A&AS, 134, 255
Kos J., Zwitter T., 2013, ApJ, 774, 72
Krelowski J., Sneden C., 1994, in Cutri R. M., Latter W. B., eds, ASP Conf. Ser. Vol. 58, The First Symposium on the Infrared Cirrus and Diffuse Interstellar Clouds. Astron. Soc. Pac., San Francisco, p. 12
Krelowski J., Snow T. P., Seab C. G., Papaj J., 1992, MNRAS, 258, 693
Lallement R., Vergely J.-L., Valette B., Puspitarini L., Eyer L., Casagrande L., 2014, A&A, 561, A91
Livio M., 1997, in Wickramasinghe D. T., Bicknell G. V., Ferrario L., eds, ASP Conf. Ser. Vol. 121, IAU Colloq. 163: Accretion Phenomena and Related Outflows. Astron. Soc. Pac., San Francisco, p. 845
Lynds B. T., 1962, ApJS, 7, 1
Mainzer A. et al., 2011, ApJ, 731, 53
Mainzer A. et al., 2014, ApJ, 792, 30
Mathew B. et al., 2018, ApJ, 857, 30
Mel'nik A. M., Dambis A. K., 2017, MNRAS, 472, 3887
Melnikov S., Woitas J., Eislöffel J., Bacciotti F., Locatelli U., Ray T. P., 2008, A&A, 483, 199
Mendigutía I., Calvet N., Montesinos B., Mora A., Muzerolle J., Eiroa C., Oudmaijer R. D., Merín B., 2011, A&A, 535, A99
Mendigutía I., Oudmaijer R. D., Rigliaco E., Fairlamb J. R., Calvet N., Muzerolle J., Cunningham N., Lumsden S. L., 2015, MNRAS, 452, 2837
Munari U., 2014, in Woudt P. A., Ribeiro V. A. R. M., eds, ASP Conf. Ser. Vol. 490, Stella Novae: Past and Future Decades. Astron. Soc. Pac., San Francisco, p. 183
Munari U., Moretti S., 2012, Balt. Astron., 21, 22
Munari U., Zwitter T., 1997, A&A, 318, 269
Munari U. et al., 2012, Balt. Astron., 21, 13
Munari U., Henden A., Frigo A., Dallaporta S., 2014, J. Astron. Data, 20, 4
Nugent C. R. et al., 2015, ApJ, 814, 117
Sale S. E. et al., 2014, MNRAS, 443, 2907
Samus' N. N., Kazarovets E. V., Durlevich O. V., Kireeva N. N., Pastukhova E. N., 2017, Astron. Rep., 61, 80
Shappee B. J. et al., 2014, ApJ, 788, 48
Stahler S. W., Palla F., 2005, The Formation of Stars. Wiley-VCH, Weinheim
Stephenson C. B., Sanduleak N., 1977, ApJS, 33, 459
Sterken C., Jaschek C., 1996, Light Curves of Variable Stars. Cambridge Univ. Press, Cambridge
Storey P. J., Hummer D. G., 1995, MNRAS, 272, 41
Tokunaga A. T., 2000, in Cox A. N., ed., Allen's Astrophysical Quantities, 4th edn. AIP Press, New York, p. 143
Torres G., 2010, AJ, 140, 1158
Vioque M., Oudmaijer R. D., Baines D., Mendigutía I., Pérez-Martínez R., 2018, A&A, 620, A128
Vos D. A. I., Cox N. L. J., Kaper L., Spaans M., Ehrenfreund P., 2011, A&A, 533, A129
Warner B., 1995, Cataclysmic Variable Stars, Cambridge Astrophysical Series, Vol. 28. Cambridge Univ. Press, Cambridge
Wisniewski W., Coyne G. V., 1976, Vatican Obs. Publ., 1, 225
Wright N. J., 2018, in Wolk S., ed., Cambridge Workshop on Cool Stars, Stellar Systems, and the Sun. p. 75, Available at: http://coolstars20.cfa.harvard.edu/
Wright N. J., Drew J. E., Mohr-Smith M., 2015, MNRAS, 449, 741
Yamashita Y., Nariai K., 1977, An Atlas of Representative Stellar Spectra. Univ. Tokyo Press, Tokyo

SUPPORTING INFORMATION

Supplementary data are available at *MNRAS* online.

Table 1. Optical photometry of VES 263.
Table 4. *B*-band magnitude of VES 263 estimated on photographic plates taken with astrographs in Crimea (C) and Sonneberg (S).

Please note: Oxford University Press is not responsible for the content or functionality of any supporting materials supplied by the authors. Any queries (other than missing material) should be directed to the corresponding author for the article.

This paper has been typeset from a TEX/LATEX file prepared by the author.